JOURNAL OF THERMOPHYSICS AND HEAT TRANSFER
Vol. 11, No. 3, July–September 1997

Instability and Heat Transfer in Grooved Channel Flow

R. S. Iyer[*] and S. Kakac[†]
University of Miami, Coral Gables, Florida 33124-0624
and
K.-Y. Fung[‡]
Hong Kong Polytechnic University, Hung Hom, Kowloon, Hong Kong

Two-dimensional laminar flow and heat transfer in a channel with periodic grooves simulating electronic components were computed by solving the Navier–Stokes and energy equations using a high-order finite difference scheme. High-order accuracy was obtained using compact-differencing for spatial derivatives. Beyond a critical Reynolds number, which varies significantly with wall geometry, the flow develops and sustains large-amplitude, time-periodic, nonlinear oscillations similar to the instability of the embeded shear layer. These oscillations enhance the heat transfer rate between the heated walls and the cooling fluid. An optimal component spacing was found to exist where the flow exhibits a substantial heat transfer enhancement with a proportionally small increase in the driving pressure drop.

Nomenclature

a = dimensionless groove depth
a_0, a_1, a_2 = coefficients for compact-differencing scheme
b_0, b_1, b_2 = coefficients for compact-differencing scheme
c_p = specific heat at constant pressure, J/kg K
c_0, c_1, c_2 = coefficients for compact-differencing scheme
d = channel half-height, m
d_0, d_1, d_2 = coefficients for compact-differencing scheme
h = heat transfer coefficient, W/m^2 K
k = thermal conductivity, W/m K
L = dimensionless length of the periodic flow domain
l = dimensionless groove length
Nu = Nusselt number, hd/k
n = iteration/temporal index; direction normal to a surface
P = pressure, Pa
Pr = Prandtl number, $\mu c_p/k$
q'' = wall heat flux, W/m^2
Re = Reynolds number, $\rho u_0 d/\mu$
r = grid stretching ratio
T = temperature, K
t = time, s
u = x component of velocity, m/s
u_0 = mean channel centerline velocity, m/s
v = y component of velocity, m/s
X = dimensionless length in x direction, x/d
x = length in x direction, m
Y = dimensionless length in y direction, y/d
y = length in y direction, m
ζ = vorticity, s^{-1}
θ = dimensionless temperature, $kT/q''d$
μ = dynamic viscosity, kg/ms
ρ = density, kg/m^3
τ = dimensionless time, u_0t/d
τ_p = dimensionless time period of oscillation, $1/\Omega$
ψ = stream function, m^2/s
Ω = dimensionless frequency of oscillation

Subscript

i = node index in the x direction

Superscripts

$*$ = dimensionless
$'$ = first derivative
$''$ = second derivative

Introduction

COOLING of electronic equipment is a constraint in the development of faster, smaller, and more reliable electronics. Over the years, the trend toward large-scale integration in microprocessors has resulted in higher heat fluxes at all levels of the electronic modules.[1] It has therefore become necessary to optimize packaging configurations for better heat transfer from these heat-producing electronic devices and to develop newer techniques for more effective heat removal. A substantial amount of experimental and numerical work has been done in this area.

Moffat et al.[2] and Lehmann and Wirtz[3] conducted forced convective air-cooling experiments in the turbulent regime with an array of discrete heat sources and heated walls, respectively, in a grooved channel. They developed correlations for heat transfer rates based on flow velocity, channel height, and component spacing. Garimella and Eibeck[4] performed similar experiments with a water-cooled configuration and an array of discrete heat sources to simulate a realistic electronic package configuration. Correlations were obtained for both laminar and turbulent convective heat transfer. There has also been some effort in studying heat transfer enhancement in laminar flows by inducing and sustaining flow instability through flow modulation. The object of this was to obtain heat transfer rates comparable to turbulent flows without the accompanying large pressure drops. Greiner[5] conducted experiments on the hydrodynamic resonance in a grooved channel geometry and studied the effect of induced flow instability on heat transfer rate in laminar flow. For a similar geometry, Ghaddar et al.[6,7] used a high-order spectral element method to compute flow and heat transfer. They showed that for a specific geometry and Reynolds numbers larger than a critical value of 9.75×10^2, the flow when perturbed, developed and sustained periodic oscillations. They also demonstrated a significant heat transfer enhancement by perturbing the mean flow with small-ampli-

---

Received Aug. 12, 1996; revision received March 31, 1997; accepted for publication March 31, 1997.

[*] Graduate Student, Department of Mechanical Engineering.

[†] Professor, Department of Mechanical Engineering.

[‡] Professor, Department of Mechanical Engineering, Senior Member AIAA.

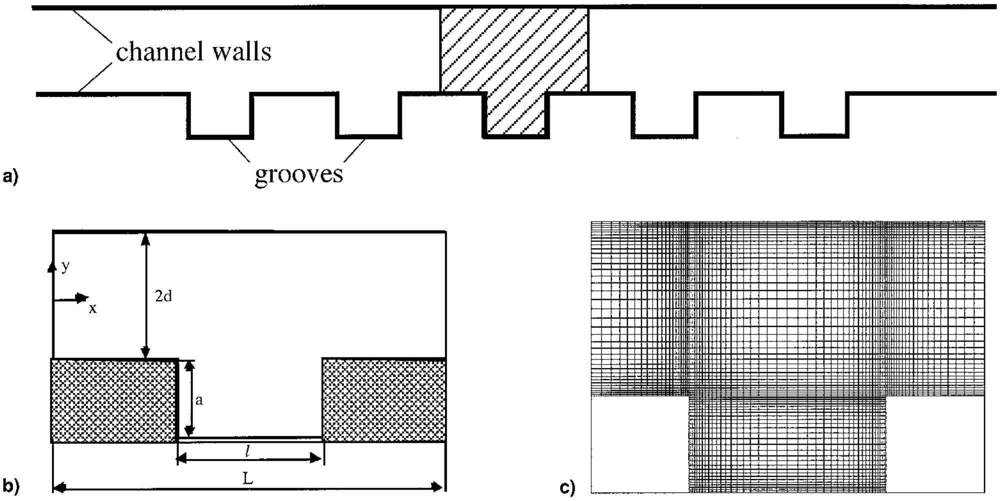

Fig. 1 a) Schematic of a grooved channel with the computational domain shaded, b) geometry of a computational unit of the flow domain, and c) a typical grid used in the simulations.

tude disturbances at resonant frequencies. Amon and Mikic,[8] Amon,[9] and Nigen and Amon[10] studied the dependency of the heat transfer characteristics on the geometry of a grooved channel and compared the relative influence of turbulence, active flow modulation, and self-induced and sustained flow instability on the enhancement of heat transfer. Though higher degrees of flow instability and, consequently, heat transfer rates could be obtained by active flow modulation, it is obvious that periodic and continuous perturbation of the flow is impractical in most cases. However, if the flow could be naturally induced in the laminar regime to sustained instability by the control of certain key flow parameters, higher heat transfer rates would be effortlessly obtained. Little effort was found in all of the previous numerical work to study self-induced oscillations and, specifically, their variations with the geometry of the channel. Here, in addition to reproducing some of the earlier numerical results, the effect of the geometry, specifically that of the groove length, on the characteristics of self-sustained flow oscillations and the heat transfer rates is studied.

From previous numerical and experimental investigations, it is apparent that the laminar flow in a channel with grooves or blocks becomes unsteady at relatively low Reynolds numbers. As can be expected, this has been shown to cause enhancement of heat transfer from the channel walls and is consequently an important and desired effect. To capture the unsteadiness in the flow, a highly accurate numerical scheme is required. To this effect only a few schemes have been used: the spectral–element method by Ghaddar et al.[6,7] and a third-order finite volume scheme by Pereira and Sousa.[11] The spectral–element method, though offering high accuracy, is extremely difficult to implement for complex flow situations. Compact-differencing, also known as Hermitian techniques, has been in limited use for a long time. In one of the earliest works, Hirsh[12] demonstrated the use of compact-differencing in fluid dynamics problems by solutions of the one-dimensional Burgers equation, the boundary-layer equation, and the steady two-dimensional driven-cavity problem. Subsequently, Adam[13] used compact-differencing to solve one-dimensional nonlinear equations and developed stencils for the first and second derivatives on a nonuniform grid. Ciment et al.[14] developed compact stencils for the combined first and second derivative terms in a one-dimensional Navier–Stokes-like equation, and reported a reduction in computational effort for the same solution accuracy. Gupta[15] and Dennis and Hudson[16] used compact-differencing to solve the one-dimensional unsteady and the two-dimensional steady Navier–Stokes-type equations. They managed to remove the derivative terms entirely and obtained the solutions by a nested iterative technique based on a nine-point formulation. In a recent work, Lele[17] studied classes of compact-difference stencils and demonstrated their accuracies by computing the solution for the spatial evolution of two supersonic mixing layers. The use of these high-order schemes, however, results in a pentadiagonal system of equations, which is computationally time consuming and requires the specification of boundary conditions at the boundary and next interior levels. Except for the supersonic mixing layer, there was no compliance of solution at a physical boundary, thus a difficulty in applying compact differencing to solving the Navier–Stokes equations is avoided. The formulation by Hirsh,[12] though, incorporated time integration of the solution, but as the author mentioned, his implementation did not ensure time accuracy. Most recently, compact-differencing techniques have been successfully used to solve wave propagation problems.[18] The inherent difficulties in using compact-differencing techniques for solving the Navier–Stokes equations are the treatment of the boundary values and their derivatives and the solution of a large system of coupled equations. Techniques adopted to tackle these difficulties are discussed in the following two sections.

Problem Formulation

Although the geometry of a grooved channel can mimic a variety of practical flow situations, the emphasis of this paper is on enhancing the heat transfer performance in electronic cooling and, consequently, appropriate references and simplifications pertaining to this were accounted for. The geometry of an electronic package is typically three dimensional and irregular. For simplicity, a channel with periodic grooves as shown in Fig. 1a is considered. At distances far from the inlet, four to five components downstream,[2] the flow is assumed to be two dimensional, hydrodynamically and thermally fully developed, and self-repeating as the grooves. Thus, only a unit of flow domain as the shaded region in Fig. 1a is considered. Figure 1b shows the geometry of the flow domain.

The governing equations for the flow are

Continuity:

$$\nabla \cdot \bar{v} = 0 \tag{1}$$

Momentum:

$$\frac{\partial \bar{v}}{\partial t} + \bar{v} \cdot \nabla \bar{v} = -\frac{1}{\rho} \nabla p + \frac{\mu}{\rho} \nabla^2 \bar{v} \tag{2}$$

Energy:

$$\frac{\partial T}{\partial t} + \bar{v}\cdot\nabla T = \frac{k}{\rho c_p}\nabla^2 T \tag{3}$$

The effects of viscous dissipation and natural convection are neglected. The thermophysical fluid properties are assumed to be constant. The equations are nondimensionalized using the channel half-height d, and the mean channel centerline velocity at the inlet, i.e.,

$$u_0 = \frac{1}{2d}\int_{-d}^{d} u(0, y)\,\mathrm{d}y$$

and cast into a stream function–vorticity form:

$$\nabla^2\psi^* = -\zeta^* \tag{4}$$

$$\frac{\partial\zeta^*}{\partial\tau} + u^*\frac{\partial\zeta^*}{\partial X} + v^*\frac{\partial\zeta^*}{\partial Y} = \frac{1}{Re}\left(\frac{\partial^2\zeta^*}{\partial X^2} + \frac{\partial^2\zeta^*}{\partial Y^2}\right) \tag{5}$$

$$\frac{\partial\theta}{\partial\tau} + u^*\frac{\partial\theta}{\partial X} + v^*\frac{\partial\theta}{\partial Y} = \frac{1}{RePr}\left(\frac{\partial^2\theta}{\partial X^2} + \frac{\partial^2\theta}{\partial Y^2}\right) \tag{6}$$

where

$$\begin{gathered} u^* = \frac{u}{u_0} \qquad v^* = \frac{v}{u_0} \qquad X = \frac{x}{d} \qquad Y = \frac{y}{d} \\ \tau = \frac{u_0 t}{d} \qquad \theta = \frac{kT}{q''d} \qquad Re = \frac{\rho u_0 d}{\mu} \qquad Pr = \frac{\mu c_p}{k} \end{gathered} \tag{7}$$

$$u^* = \frac{\partial\psi^*}{\partial Y} \qquad v^* = -\frac{\partial\psi^*}{\partial X} \tag{8}$$

$$\zeta^* = \frac{\partial v^*}{\partial X} - \frac{\partial u^*}{\partial Y} \tag{9}$$

The pressure term is thus eliminated and can be recovered from the vorticity and stream function fields at any time. Here, only the pressure drop across the flow domain is of practical interest. A boundary-layer-type order-of-magnitude analysis of the governing equations led to the following simplified expression for the dimensionless pressure P^*:

$$\frac{\partial u^*}{\partial\tau} = -\frac{1}{2}\frac{\partial P^*}{\partial X} + \frac{1}{Re}\frac{\partial^2 u^*}{\partial Y^2}$$

where

$$P^* = \frac{P}{(1/2)\rho u_0^2} \tag{10}$$

which can be integrated over time and space for the average pressure drop. The superscript *, denoting dimensionless variables, will be omitted for simplicity; and all variables encountered from this point on are dimensionless unless mentioned otherwise.

The channel walls as streamlines themselves are assigned constant stream function values: $\psi = 1$ along the top wall and $\psi = 0$ along the bottom wall. The stream function at the inlet and exit is assumed periodic, i.e.,

$$\psi_{x=0} = \psi_{x=L}$$

The vorticity values at the channel walls where the velocity components satisfy the no-slip condition are computed according to the following formulas:

$$\zeta = -\frac{\partial u}{\partial Y} \quad \text{or} \quad \zeta = -\frac{\partial^2\psi}{\partial Y^2}$$

for walls parallel to the x axis.

Similarly

$$\zeta = \frac{\partial v}{\partial X} \quad \text{or} \quad \zeta = -\frac{\partial^2\psi}{\partial X^2}$$

for walls parallel to the y axis.

As with the stream function, the vorticity values are identical at the inlet and exit, i.e.,

$$\zeta_{x=0} = \zeta_{x=L}$$

The bottom channel wall is subject to a constant heat flux, while the top channel wall is treated as adiabatic. Unlike vorticity and stream function, the temperature increases in the streamwise direction because of heat addition from the components. Nevertheless, in the thermally developed flow regime, the temperature can be split into a static component that increases uniformly in the streamwise direction as a result of heat addition and a periodic component that fluctuates with the geometry,[6,7] i.e.,

$$\theta_{x=L} = \theta_{x=0} + \frac{(L + 2a)/d}{RePr}$$

$(L + 2a)/d$ is the total dimensionless heated length of the channel wall in the flow domain considered. Thus, the periodic component of the temperature field θ is identical at the inlet and exit, i.e.,

$$\theta_{x=0} = \theta_{x=L}$$

The thermal boundary conditions for the channel walls reduce to the following: $\partial\theta/\partial n = 1$ for the bottom wall (constant heat flux) and $\partial\theta/\partial n = 0$ for the top wall (adiabatic), where n denotes the direction normal to the wall.

Solution Method

The governing equations are discretized using high-order compact-differencing and the solution is advanced in the time direction. A rectangular nonuniform grid (Fig. 1c) with a fine spacing of 0.015 dimensionless units close to the walls and a stretching factor of approximately 1.1 are used.

Compact-Differencing Technique

Compact-differencing is a high-order finite differencing technique in which the function values and their spatial derivatives at the neighboring points are related. A typical compact-differencing stencil for the first derivative is

$$a_0 f'_{i-1} + a_1 f'_i + a_2 f'_{i+1} = \frac{b_0 f_{i-1} + b_1 f_i + b_2 f_{i+1}}{\Delta x_i} \tag{11a}$$

where the coefficients a_0, a_1, a_2, b_0, b_1, and b_2 are functions of the local grid spacing, $\Delta x_i = x_i - x_{i-1}$ (e.g., Ref. 15). They are conveniently expressed here in terms of the local grid expansion ratio r:

$$a_0 = r^2 \quad a_1 = (r + 1)^2 \quad a_2 = 1$$

$$b_0 = -\frac{2r^2(r + 2)}{r + 1} \quad b_1 = \frac{2(r + 1)^2(r - 1)}{r} \quad b_2 = \frac{4r + 2}{r(r + 1)}$$

where

$$r = \Delta x_{i+1}/\Delta x_i \tag{11b}$$

and similarly for the second derivative

$$c_0 f''_{i-1} + c_1 f''_i + c_2 f''_{i+1} = \frac{d_0 f_{i-1} + d_1 f_i + d_2 f_{i+1}}{\Delta x_i^2} \tag{12a}$$

expressed as

$$\begin{gathered} c_0 = \frac{r(1 - r^3 + 2r)}{12(r + 1)} \quad c_1 = \frac{(r^4 + 5r^3 + 8r^2 + 5r + 1)}{12(r + 1)} \\ c_2 = -\frac{r^3 + 2r^2 + 2}{12(r + 1)} \quad d_0 = -(r + 1) \quad d_1 = r \quad d_2 = 1 \end{gathered} \tag{12b}$$

The truncation error of the previous approximation for the first derivative has a leading term proportional to $(\Delta x_i)^4 f_i^v$, and that for the second derivative proportional to $(\Delta x_i)^3 f_i^v$. Thus, the three-point compact-differencing scheme offers at least a third-order accuracy for computing up to the second spatial derivative on a nonuniform grid, which is a substantial reduction of numerical dissipation and dispersion inherent to lower-order finite difference schemes. Higher levels of accuracy can be obtained with stencils having larger data bandwidths, but at the expense of substantially lower solution efficiencies and increased difficulties in specifying consistently accurate boundary conditions.

Numerical Scheme

The vorticity transport equation is split and solved in an alternating direction implicit (ADI) fashion with the convective terms expressed explicitly using the three-level Adams–Bashforth formulation and the diffusive terms implicitly using the Crank–Nicolson scheme, i.e.,

$$\begin{aligned} &\frac{\partial \zeta^{n+1/2}}{\partial \tau} + \left(\frac{3}{2}\frac{\partial \zeta^n}{\partial X} - \frac{1}{2}\frac{\partial \zeta^{n-1/2}}{\partial X}\right) + \left(\frac{3}{2}\frac{\partial \zeta^n}{\partial Y} - \frac{1}{2}\frac{\partial \zeta^{n-1/2}}{\partial Y}\right) \\ &\quad = \frac{1}{2Re}\left(\frac{\partial^2 \zeta^{n+1/2}}{\partial X^2} + \frac{\partial^2 \zeta^n}{\partial X^2}\right) + \frac{1}{Re}\frac{\partial^2 \zeta^n}{\partial Y^2} \\ &\frac{\partial \zeta^{n+1}}{\partial \tau} + \left(\frac{3}{2}\frac{\partial \zeta^{n+1/2}}{\partial X} - \frac{1}{2}\frac{\partial \zeta^n}{\partial X}\right) + \left(\frac{3}{2}\frac{\partial \zeta^{n+1/2}}{\partial Y} - \frac{1}{2}\frac{\partial \zeta^n}{\partial Y}\right) \\ &\quad = \frac{1}{Re}\frac{\partial^2 \zeta^{n+1/2}}{\partial X^2} + \frac{1}{2Re}\left(\frac{\partial^2 \zeta^{n+1}}{\partial Y^2} + \frac{\partial^2 \zeta^{n+1/2}}{\partial Y^2}\right) \end{aligned} \tag{13}$$

The vorticity transport equation is thus reduced to two sets of equations having a tridiagonal data structure that can be solved efficiently, but in each of the ADI steps a large amount of computation is also required for evaluating the convective and diffusive terms according to the compact formulas, Eqs. (11) and (12). This is compensated for by the high solution accuracy rendered on relatively coarse grids. The Poisson equation, Eq. (4), is discretized to the same level of accuracy using a nine-point stencil and solved by Gauss–Seidel iterations until convergence is reached with a maximum relative change in the stream function values between successive iterations of less than 0.01%.

Unlike the formulation of Hirsh,[12] where the convective terms were implicitly solved as a computationally intensive block tridiagonal equation system, the explicit Adams–Bashforth time-extrapolation of the convective terms used here requires only the solution of simple tridiagonal systems, but places a restriction on the maximum time step for numerical stability. The time steps used for the present work were of the order of 10^{-3} dimensionless units or correspondingly a Courant number of 0.3.

The use of the ADI formulation may introduce nonphysical quantities at half-steps and caution must be taken to ensure that at these steps physically meaningful boundary conditions are being enforced. Here, vorticity values extrapolated from previous time instances are used for solving the stream function values. The overall accuracy of the formulation is therefore of $\mathcal{O}(\Delta t^2, \Delta x^3)$. However, since for high Reynolds number flows the importance of the diffusive terms is confined to thin layers near the walls and the shear-layer, the predominant convective terms are practically fourth-order accurate over the rest of the flow region.

Boundary Point Stencils

For computing the function values and their derivatives at boundary points, one-sided compact-differencing-like formulations one order less accurate than the corresponding stencil for interior points are incorporated. The stencils for the three kinds of derivative boundary conditions encountered in the present study are as follows.

Second derivative with a nonzero first derivative at the boundary:

$$f''_0 + \frac{r + 2}{r + 1} f''_1 = -\frac{6}{\Delta x_1^2}\left(\frac{1}{r^2 - 1} f_0 + \frac{1}{r^2 - r} f_1 - \frac{1}{r^3 - r} f_2\right) \tag{14}$$

where the subscripts 0, 1, and 2 refer to the wall and its two adjacent interior points, respectively.

Second derivative with a zero first derivative:

$$2f''_0 + f''_1 = -\frac{6}{\Delta x_1^2}(f_0 - f_1) \tag{15}$$

First derivative:

$$f'_0 + f'_1 = -\frac{2}{\Delta x_1}(f_0 - f_1) \tag{16}$$

Nusselt Number

In the present work, only the time- and space-averaged Nusselt number used by Ghaddar et al.[7] as a measure of heat transfer performance is computed, i.e.,

$$Nu = \frac{(L + 2a)^2/L}{\int_{\text{bottom wall}} [\theta_{\text{wall}} - \theta_{\text{ref}}]} \tag{17}$$

where the reference mixed-mean-temperature θ_{ref} at the inlet is defined to have easy comparison with corresponding measured values in experiments:

$$\theta_{\text{ref}} = \frac{3}{4}\int_{-1}^{1} u(y)\theta(y)\, \mathrm{d}y(x = 0)$$

Numerical Error

The numerical scheme, as mentioned earlier, has an overall third-order accuracy in space and second-order accuracy in time. Simulations with grids of various degrees of coarseness were conducted to determine the required resolution for grid-independent solutions. The exact solution for the problem is not known, and so the maximum error is estimated to be about 2% by comparing the solutions on regular and fine grids with twice the grid points. The same grid is used for flows with comparable Reynolds numbers. A few solutions presented here were computed with half the time step to ensure consistence and time-step independence.

Results

First, the results for configurations similar to those of Ghaddar et al.[6,7] are presented to validate the numerical scheme. Second, the results for a different geometry demonstrating the variation of the stability boundary and the effects of linear and

Table 1 Comparison of the most amplified frequencies Ω

Geometry (a = 1.1111, Re = 5.25 × 10^2)	Ω, present work	Ω, Ghaddar et al.[6]
L = 6.6666, l = 2.2222	0.143	0.142
L = 5.5554, l = 2.7777	0.074	0.07
L = 4.4444, l = 2.2222	0.1	0.1
L = 3.0, l = 1.5	0.148	0.154

Table 2 Comparison of Nusselt numbers

Re	Nu, present work	Nu, Ghaddar et al.[7]
2.25 × 10^2	0.98	~1.1
5.25 × 10^2	1.07	1.12

nonlinear flow instabilities are studied and presented. Finally, the heat transfer characteristics of geometries with different groove lengths are presented, and the effect of nonlinear instability on heat transfer enhancement is discussed.

Reproduction of Earlier Results

To compare the accuracy of the scheme and validate subsequent results, simulations were performed first for geometries identical to those used by Ghaddar et al.[6] Steady flows were computed into which small perturbations were introduced to identify the most amplifying (least damping) frequency as the geometry varies (L from 6.6666 to 3.0 and l from 2.2222 to 1.5). A comparison of these frequencies showing excellent agreement is presented in Table 1. For the baseline geometry (L = 6.6666, l = 2.2222, and a = 1.1111), the critical Reynolds number marking the onset of amplification of disturbances determined by Ghaddar et al.[6] was 9.75 × 10^2, and the present method predicted sustain periodic oscillations at a Reynolds number of 1 × 10^3, thus confirming their results and validating the accuracy of the present numerical scheme. The Nusselt numbers at two Reynolds numbers (2.25 × 10^2 and 5.25 × 10^2) were computed and compared in Table 2 with those from Ghaddar et al.[7] for L = 6.6666, l = 2.2222, and a = 1.1111, showing again a good agreement. No effort was made to account for the small quantitative differences (less than 10%) in these predictions.

In addition, the scheme was also adapted to compute the flow and heat transfer characteristics for geometries similar to experiments conducted by Li et al.[19] The numerical simulations were consistent with measurements from the experiments.

Onset of Instability

The baseline geometry in the present work, L = 4.4444, l = 2.2222, and a = 1.1111, differs from the one used by Ghaddar et al.,[6,7] in that the distance separating the grooves is smaller by half. The reason for choosing this slightly different geometry was to study the effect of geometry on the stability boundary and to have a smaller computational domain and, consequently, fewer computational resources.

Over a range of Reynolds numbers steady flows were computed and perturbed slightly with a perturbation of about 5% of the mean flow. In all subsequent flow fluctuation studies, the y-velocity component at the middle of the channel inlet (x = 0, y = 0) was monitored as a flow stability measure. Figure 2a shows the decay of the imposed perturbation with time for Re = 5.25 × 10^2, and Fig. 2b shows a slower decay for 7.25 × 10^2. The amplification rate of these perturbations suggests a linear dependency and when extrapolated becomes positive at Re = 7.65 × 10^2, beyond which the flow would amplify the slightest disturbance containing the resonant frequency and become unstable. As expected, the flow computed for Re = 8 × 10^2 developed instability and sustained periodic oscillations (Fig. 2c). Between the regimes of stable and unstable flows, there lies a region of neutral stability where the flow when slightly perturbed would return to a steady state, but if the flow was significantly perturbed it would transit into the unstable region and develop sustained oscillations. It was found that the steady flow at Re = 7.25 × 10^2 developed sustained oscillations in a manner similar to the flow shown in Fig. 2c, when perturbed disturbances exceed 10% of the mean flow.

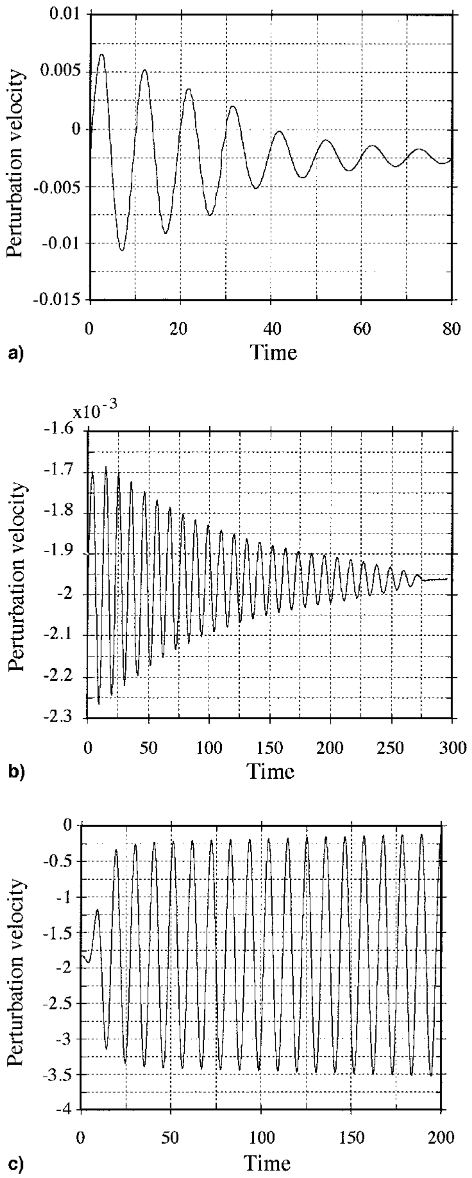

Fig. 2 Perturbations in flow measured by the y component of the inlet centerline velocity at x = 0 y = 0, showing decreasing stability with increasing Re = a) 5.25 × 10^2, b) 7.25 × 10^2, and c) 8 × 10^2 for L = 4.4444, l = 2.2222, and a = 1.1111.

The results presented previously show a reduced critical Reynolds number from 1 × 10^3 to 7.65 × 10^2 as L is reduced from 6.6666 to 4.4444, confirming quantitatively that the flow tends to be less stable for smaller L.[6]

Nature of Instability

This section describes the transition from a steady flow to its nonlinear unstable state. The results obtained here help explain the heat transfer dependence on the geometry in the next section, for which the geometry was chosen. As shown in later sections, the analysis is, nonetheless, general and applicable to similar flows.

For L = 5.5555, l = 3.3333, a = 1.1111, and a supercritical Re = 6.5 × 10^2, the flow develops self-sustained periodic os-

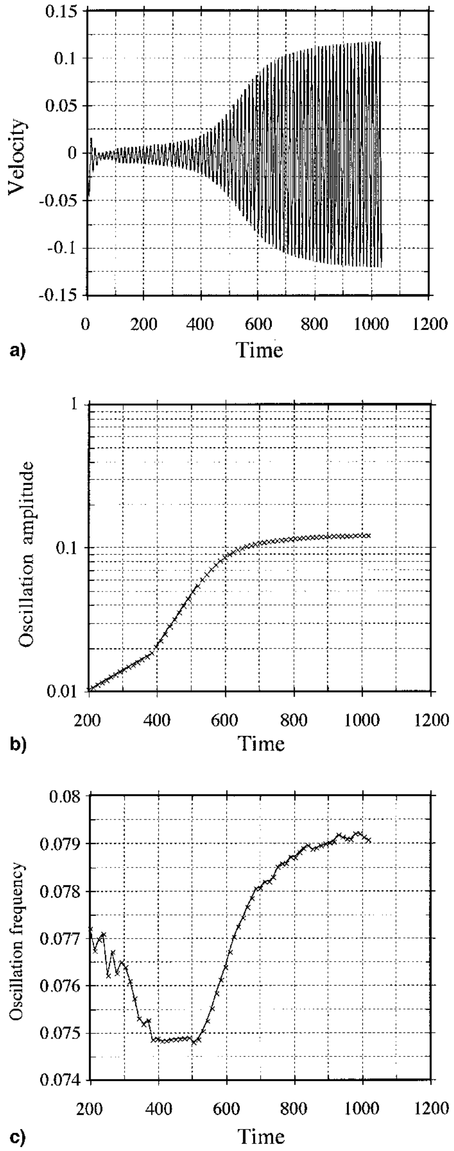

Fig. 3 Sustained velocity oscillations and their a) amplitude, b) frequency, and c) variations with time for $Re = 6.5 \times 10^2$, L = 5.5555, l = 3.3333, and a = 1.1111.

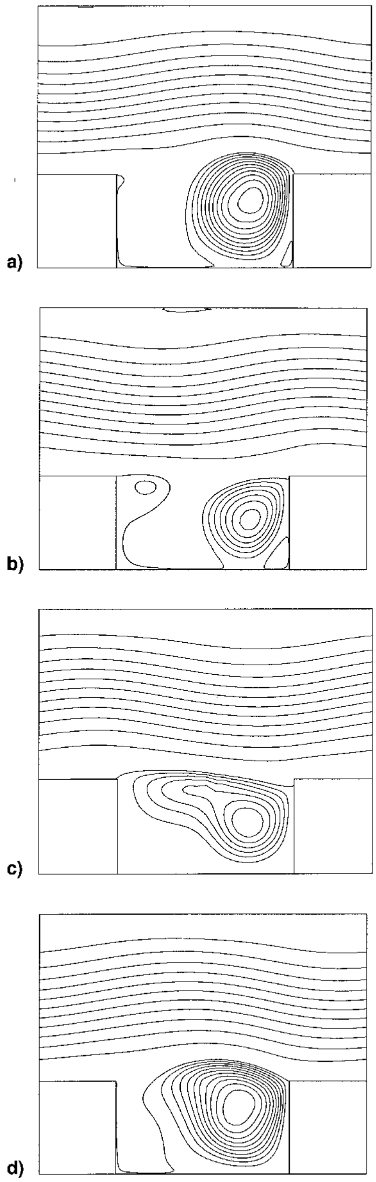

Fig. 4 Streamlines depicting flow at four instances. t = a) 0, b) $2\tau_p/7$, c) $4\tau_p/7$, and d) $6\tau_p/7$, during one period of oscillation for $Re = 6.5 \times 10^2$, L = 4.7777, l = 2.5, and a = 1.1111.

cillations. Figure 3a shows the three distinct stages of development of the velocity at the reference point as a function of time: 1) the initial decay of the imposed oscillations, 2) the exponential growth of the flow oscillations, and 3) the reduction of amplification rate to oscillations with a constant amplitude. In the first stage, since the initial perturbation was introduced at no specific frequency, there is a decay of the components of perturbation with frequencies far removed from the most amplified frequency and the oscillations corresponding to the most amplified frequency of the flow become dominant. Excluding the decays in the first stage, Figure 3b shows the variation of the amplitude of oscillation with time on a semilog scale. An analysis of the amplification indicates two distinct exponential rates of growth of the oscillation amplitude. The transition from the slower to the faster growth rate occurs at about t = 400. Beyond about t = 530, the growth rate deviates from exponential as the amplitude of oscillation approaches a constant. Figure 3c shows the variation of the average frequency of two cycles of oscillation with time. The variation of the flow frequency from cycle to cycle is not smooth, especially in the initial stage, because of the different rates of decay for different frequencies of oscillation and the discrete nature of the data. It is seen that the frequency shifts from higher values to, and stays at, the most amplified frequency of about 0.075 Hz for a period of time, and then moves monotonously toward a higher value of about 0.079 Hz. A comparison of Fig. 3b and Fig. 3c shows the slower amplification rate lasts until the oscillations settle to the most amplified natural frequency of about 0.075 Hz. As expected, the amplification rates are substantially lower for oscillations at frequencies other than the natural frequency. At around t = 530, the amplitude of oscillations becomes large enough to cause a breakdown of the shear layer, which has remained intact until this stage. Typical flow patterns spanning one cycle of oscillation are shown in Fig. 4. This breakdown of the shear layer causes the flow to transcend from the linear instability regime to that of nonlinear instability as characterized by the deviation from the exponential growth at about t = 530 in Fig. 3b. In the regime of nonlinear instability, the flow experiences a gradual shift of the natural frequency to 0.079 Hz. Ghaddar et al.[7] also observed this shift in the frequency of the most amplified oscillations in their experiments with externally induced and sustained flow oscillations, and reported similar frequency shifts as the oscillation amplitude increased. A different study with L = 4.7777, l = 2.5, a = 1.1111, and $Re = 6.5 \times$

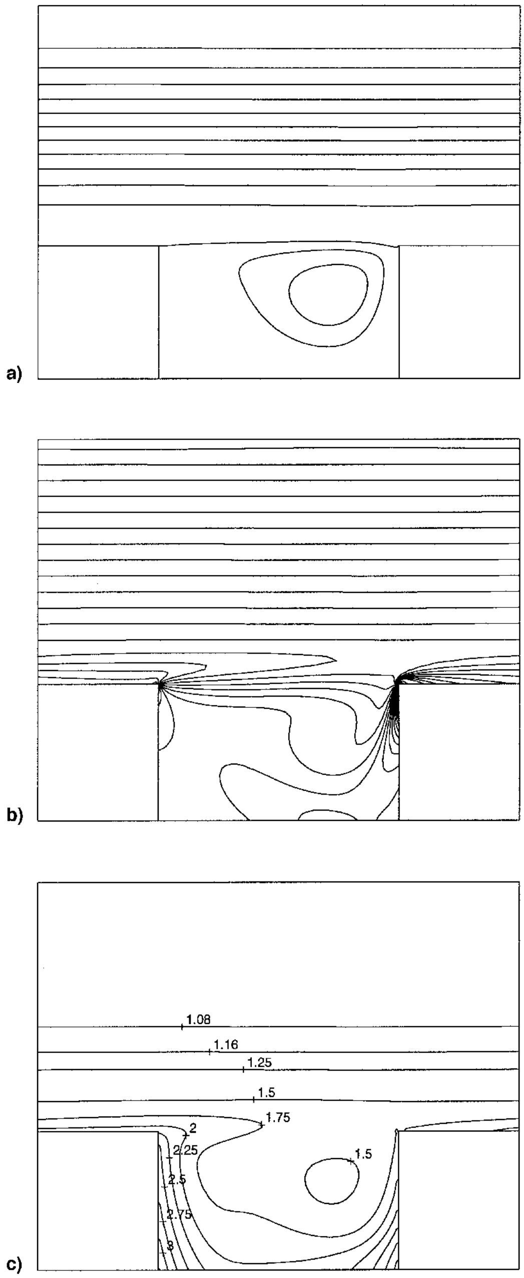

Fig. 5 a) Streamlines, b) vorticity contours, and c) temperature contours for a steady flow of $Re = 6.5 \times 10^2$, $L = 4.4444$, $l = 2.2222$, and $a = 1.1111$.

10^2, showing an identical pattern of flow development, confirms this natural process of onset of nonlinear instability for the kind of geometry discussed.

Heat Transfer Results

The emphasis in electronic packaging is the arrangement of heat-generating components of given dimensions in a way to ensure maximum heat removal. To this aim, the parameters to be specified are the space between components, the distance between circuit boards, and the flow velocity measured by Re. Some effects of these parameters on the heat removal rates had previously been investigated. Ghaddar et al.[6] reported that the resonant frequency for any geometry was not dependent on the depth of the groove and cited supporting experimental work for their observation. Consequently, similar investigations were not conducted in this paper. Ghaddar et al.[6] also mentioned, with experimental support, that increasing the groove length tends to destabilize the flow. Thus, it can be expected that increasing l beyond a certain point for a fixed Re would promote self-induced instability, and consequently, yield higher heat transfer rates. Here, the range of l was chosen from 1.1111 to 4.4444 with a fixed component length $L - l = 2.2222$. A Reynolds number of 6.5×10^2 was chosen such that the flow would vary from stable to unstable states as the component l increases, and the Prandtl number was assumed unity.

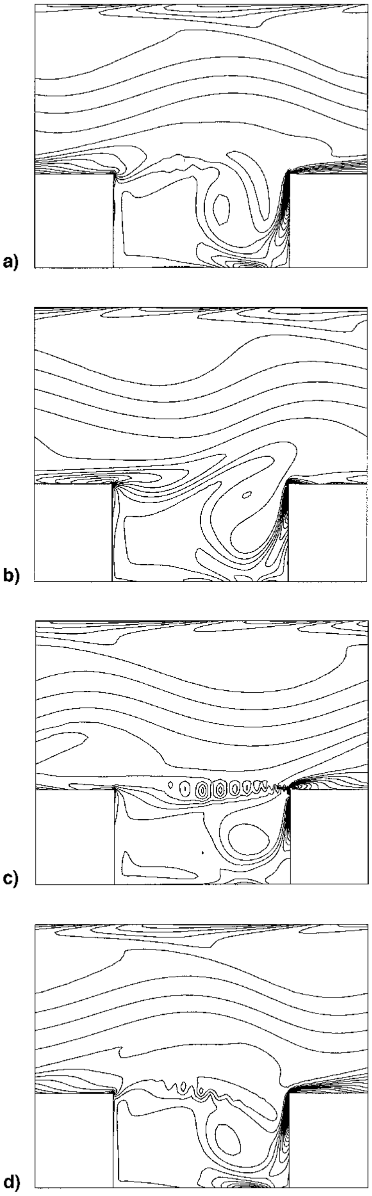

Fig. 6 Vorticity contours at four instances. t = a) 0, b) $2\tau_p/7$, c) $4\tau_p/7$, and d) $6\tau_p/7$, during one period of oscillation for $Re = 6.5 \times 10^2$, $L = 4.7777$, $l = 2.5$, and $a = 1.1111$.

The flow is steady up to $l = 2.2222$. The streamlines, vorticity, and the temperature fields for this flow are shown in Figs. 5a, 5b, and 5c, respectively. There is a pronounced shear layer across the groove lip according to the steep gradients in both the streamline and vorticity contours. The channel flow profile is very similar to the Poiseuille flow in a plane channel. A comparison of the velocity magnitudes in the channel and the groove regions reveals a very weak vortex in the groove. The streamline density in the groove region is 10 times that in the channel region. It is obvious from the stable shear layer that there is very little communication between the bulk channel flow and the groove vortex, and the only means of heat removal from the groove vortex is by conduction across this

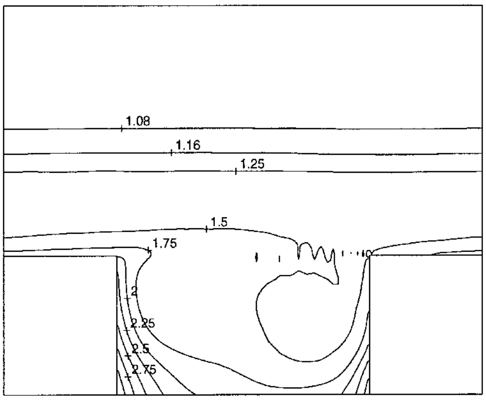

Fig. 7 **Time-averaged isotherms showing enhanced heat transfer for $Re = 6.5 \times 10^2$, $L = 4.7777$, $l = 2.5$, and $a = 1.1111$.**

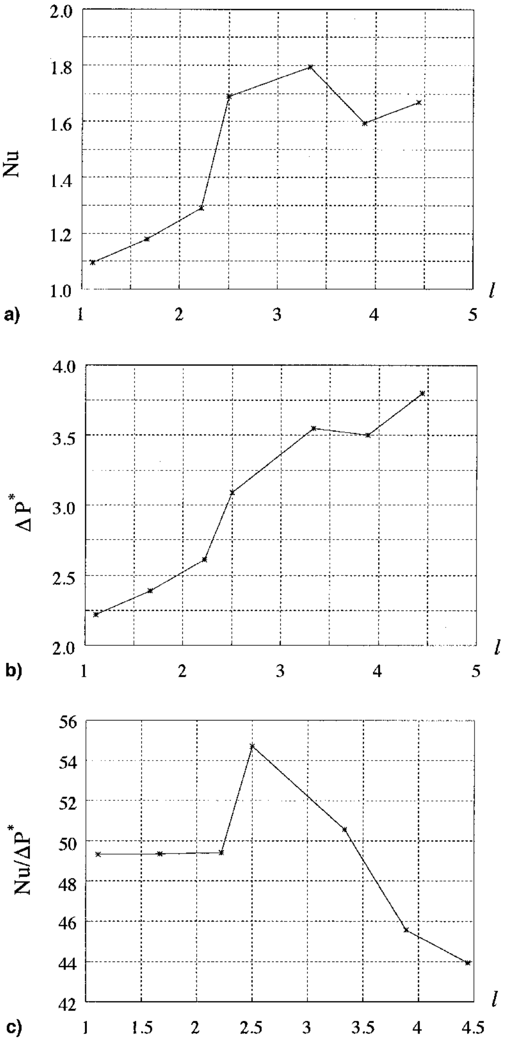

Fig. 8 **Variation of a) Nusselt number, b) dimensionless pressure drop, and c) Nusselt number per unit pressure drop with increasing groove length l.**

shear layer. This is seen in the high-temperature gradients normal to the surface of the heat-generating element and across the shear layer in Fig. 5c. This results in high temperatures in the groove region and the groove walls. For $l = 2.5$, the flow becomes unsteady and assumes a time-periodic structure as shown in Fig. 4 by the streamlines at four instances of a period of oscillation. Figure 6 shows the corresponding vorticity contours. The frequency of the oscillation is 0.096 Hz. It is seen that the shear layer is destabilized and that the bulk channel flow periodically breaks down the shear layer and ejects parts of the groove vortex. During this stage, the interactions between the bulk channel flow and the groove vortex reduce the size of the groove vortex core, increase the flow velocities in the core, enhance, consequently, the heat transfer in the core,

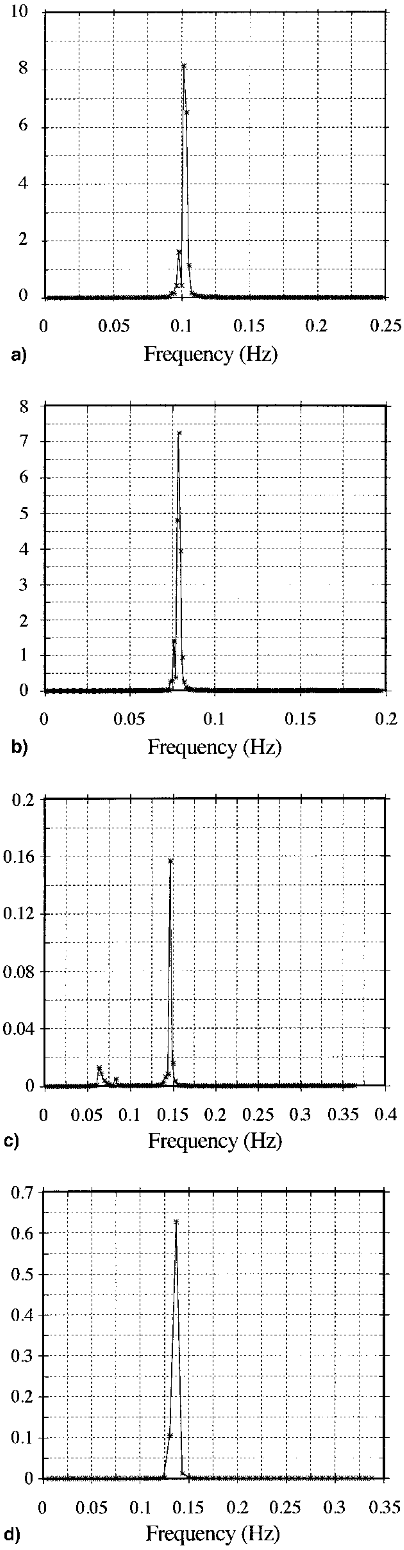

Fig. 9 **Energy levels of Fourier components for flows with self-sustained oscillations showing shifting of dominant frequencies with increasing l from a) $l = 2.5$, $L = 4.7777$; b) $l = 3.3333$, $L = 5.5555$; c) $l = 3.8888$, $L = 5.0$; and d) $l = 4.4444$, $L = 6.6666$ for $Re = 6.5 \times 10^2$ and $a = 1.1111$.**

and result in lower fluid and wall temperatures in the groove as seen from the time-averaged isotherms in Fig. 7.

These results are summarized in the variations of Nusselt number in Fig. 8a and the normalized pressure drop Δp^* in Fig. 8b with l. Increasing l, in general, corresponds to increasing Nu and Δp^* across the flow region. This trend has been observed experimentally by Moffat et al.,[2] Lehmann and Wirtz,[3] Garimella and Eibeck,[4] and other researchers and has been attributed to the increase in the heat transfer length across the shear layer. When the flow becomes unstable for $l > 2.2222$, the heat transfer rate is substantially higher because of the breakdown and interactions of the groove vortex with the bulk channel flow. The increase in Nu continues up to $l = 3.3333$, suggesting the presence of an optimum component spacing for a maximum heat removal rate. What is of greater consequence is that this increase is not accompanied by a corresponding increase in Δp^*. Figure 8c shows that the $Nu/\Delta p^*$ ratio has a constant value for $l < 2.2222$, the critical length for stable flow, suggesting that both the increases in heat transfer and pressure drop are caused by the longer flow domain. It also reveals a distinct peak in $Nu/\Delta p^*$ and identifies the optimum l at 2.5, beyond which the ratio drops dramatically.

A Fourier analysis of the oscillatory flow velocity was performed and the results are presented in Fig. 9. It is seen in Figs. 9a and 9b that the fundamental frequency of the self-sustained flow oscillations decreases with increasing l. At $l = 3.8889$ (Fig. 9c), the flow exhibits two dominant frequencies and correspondingly two dominant modes of oscillation. The predominant frequency of oscillation at 0.15 Hz is a large jump from the corresponding frequency of 0.079 Hz for $l = 3.3333$. The latter is closer to the less dominant frequency of 0.067 Hz. For $l = 4.4444$ (Fig. 9d), the flow exhibits a single dominant frequency of a lower value at 0.14 Hz and a wave number of 2. It is seen that there is an abrupt transition of flow structure at a critical l to that with a wave number of 2. All peak values in $Nu/\Delta p^*$ in similar numerical experiments with different sets of parameters have been found at the largest component length for which the wave number is 1.

Conclusions

A high-accuracy numerical scheme based on compact-differencing is successfully adapted to solve the two-dimensional Navier–Stokes equations for the flow and heat transfer in a grooved channel geometry. The accuracy of the scheme is validated by comparing with results from published numerical work. It is found that for Reynolds numbers beyond a critical value, depending sensitively on the geometry, the flow develops and sustains periodic oscillations that lead to heat transfer enhancement. The growth of these oscillations and transition from a linearly unstable to a nonlinear unstable flow occur in four stages: 1) the culmination of the most amplified unstable mode from board-banded disturbances, 2) the exponential growth of the most amplified unstable mode, 3) the destruction of the disturbance-amplifying mean shear layer by the amplified large disturbances, and 4) the cyclic formation and self-destruction of large unstable disturbances. A distinct peak in $Nu/\Delta p^*$ is found in our numerical experiments. This peak suggests the optimum distance for the placement of heating elements for heat transfer in an electronic package without a substantial penalty in increased pressure drop is that for which only the fundamental mode of instability is excited.

References

[1] Chu, R. C., "Heat Transfer in Electronic Systems," *Cooling of Electronic Systems*, edited by S. Kakac, H. Yüncü, and K. Hijikata, Kluwer Academic, Norwell, MA, 1993, pp. 71–95.

[2] Moffat, R. J., Arvizu, D. E., and Ortega, A., "Cooling Electronic Components: Forced Convection Experiments with an Air-Cooled Array," *Heat Transfer in Electronic Equipment–1985*, edited by S. Oktay and R. J. Moffat, Vol. 48, American Society of Mechanical Engineers, New York, 1985, pp. 17–27.

[3] Lehmann, G. L., and Wirtz, R. A., "The Effect of Streamwise Spacing and Length on Convection from Surface Mounted Rectangular Components," *Heat Transfer in Electronic Equipment–1985*, edited by S. Oktay and R. J. Moffat, Vol. 48, American Society of Mechanical Engineers, New York, 1985, pp. 39–47.

[4] Garimella, S. V., and Eibeck, P. A., "Heat Transfer Characteristics from an Array of Protruding Elements in a Single Phase Forced Convection, *International Journal of Heat and Mass Transfer*, Vol. 33, No. 12, 1990, pp. 2659–2669.

[5] Greiner, M., "An Experimental Investigation of Resonant Heat Transfer Enhancement in Grooved Channels," *International Journal of Heat and Mass Transfer*, Vol. 34, No. 6, 1991, pp. 1383–1390.

[6] Ghaddar, N. K., Korczak, K. Z., and Mikic, B. B., "Numerical Investigation of Incompressible Flow in Grooved Channels. Part 1. Stability and Self-Sustained Oscillations," *Journal of Fluid Mechanics*, Vol. 163, 1986, pp. 99–127.

[7] Ghaddar, N. K., Magen, M., Mikic, B. B., and Patera, A. T., "Numerical Investigation of Incompressible Flow in Grooved Channels. Part 2. Resonance and Oscillatory Heat Transfer Enhancement," *Journal of Fluid Mechanics*, Vol. 168, 1986, pp. 541–576.

[8] Amon, C. H., and Mikic, B. B., "Numerical Prediction of Convective Heat Transfer in Self-Sustained Oscillatory Flow," *Journal of Thermophysics and Heat Transfer*, Vol. 4, No. 2, 1990, pp. 239–246.

[9] Amon, C. H., "Heat Transfer Enhancement by Flow Destabilization in Electronic Chip Configurations," *Journal of Electronic Packaging*, Vol. 114, 1992, pp. 35–40.

[10] Nigen, J. S., and Amon, C. H., "Forced Convective Cooling Enhancement of Electronic Package Configurations Through Self-Sustained Oscillatory Flows," *Journal of Electronic Packaging*, Vol. 115, 1993, pp. 357–365.

[11] Periera, J. C. F., and Sousa, J. M. M., "Finite Volume Calculations of Self-Sustained Oscillations in a Grooved Channel," *Journal of Computational Physics*, Vol. 106, 1993, pp. 19–29.

[12] Hirsh, R. S., "Higher Order Accurate Difference Solutions of Fluid Mechanics Problems by a Compact Differencing Technique," *Journal of Computational Physics*, Vol. 19, 1975, pp. 90–109.

[13] Adam, Y., "A Hermitian Finite Difference Method for the Solution of Parabolic Equations," *Computers and Mathematics with Applications*, Vol. 1, 1975, pp. 393–406.

[14] Ciment, M., Leventhal, L. H., and Weinberg, B. C., "The Operator Compact Implicit Method for Parabolic Equations," *Journal of Computational Physics*, Vol. 85, 1978, pp. 135–166.

[15] Gupta, M. M., "High Accuracy Solutions of Incompressible Navier-Stokes Equations," *Journal of Computational Physics*, Vol. 93, 1991, pp. 343–359.

[16] Dennis, S. C. R., and Hudson, J. D., "Compact h^4 Finite Difference Approximation to Operators of the Navier-Stokes Type," *Journal of Computational Physics*, Vol. 85, 1989, pp. 390–416.

[17] Lele, S. K., "Compact Finite Difference Schemes with Spectral-Like Resolution," *Journal of Computational Physics*, Vol. 103, 1992, pp. 16–42.

[18] Fung, K.-Y., Man, R. S. O., and Davis, S., "An Implicit High-Order Compact Algorithm for Computational Acoustics," *AIAA Journal*, Vol. 34, No. 10, 1996, pp. 2029–2037.

[19] Li, W., Kakaç, S., Hatay, F. F., and Oskay R., "Experimental Study of Unsteady Forced Convection in a Duct with and Without Arrays of Block-Like Electronic Components," *Wärme- und Stoffübertragung*, Vol. 28, 1993, pp. 69–79.